

link to the formal publication:

<https://doi.org/10.1016/j.optcom.2018.11.057>

Multilayered Maxwell's fisheye lens as waveguide crossing

M. M. Gilarlue^a, J. Nourinia^a, Ch. Ghobadi^a, S. Hadi Badri^{b,*}, H. Rasooli Saghai^c

^a Department of Electrical Engineering, Urmia University, Urmia 57153, Iran

^b Department of Electrical Engineering, Azarshahr Branch, Islamic Azad University, Azarshahr, Iran

^c Department of Electrical Engineering, Tabriz Branch, Islamic Azad University, Tabriz, Iran

Corresponding author.

* E-mail addresses: sh.badri@iaut.ac.ir

Abstract

The Maxwell's fisheye (MFE) lens, due to its focusing properties, is an interesting candidate for implementing the crossing of multiple waveguides. The MFE lens is implemented by two different structures: concentric cylindrical multilayer and radially diverging gourd-shaped rods. Realization of the refractive index profile of the lens is achieved by controlling the thickness ratio of the alternating Si and SiO₂ layers determined by effective medium theory. Both structures are optimized to cover the entire C-band in the single mode implementation. The transmission efficiency of the ring-based structure is superior to the radial-based implementation, however, the radial-based structure almost covers the entire U-band as well. Other communication bands are partially covered in both cases. Full-wave simulations prove that the performance of multimode waveguide crossing based on the MFE lens with a radius of $2.32\ \mu\text{m}$ is promising with the average insertion loss of 0.17dB and crosstalk levels below -24.2dB in the C-band for TM₀ and TM₁ modes. The multimode intersection almost covers the entire C, L, and U bands of optical communication.

Keyword

Photonic Crystal; Multimode waveguide crossing; Maxwell's fisheye lens; Multilayer Metamaterial; Gradient index lens; effective medium theory

1. Introduction

The crossing of multiple waveguides at one intersection is inevitable in the highly dense photonic integrated circuits (PICs) where numerous devices are integrated in a very small area. An intersection with desired performance should have low insertion loss, low reflection, low crosstalk, and broad bandwidth. Various methods have been proposed for designing the intersection of two

waveguides for photonic crystals (PhCs) including utilization of single defect with doubly degenerate modes in square lattice [1]. The intersection designed with this method has narrow bandwidth and simultaneous crossing of two signals with the same wavelength causes interference [2]. To overcome these limitations coupled cavity waveguides were proposed in triangular lattice [2]. Utilization of coupled cavity waveguides generates leakage in vertical direction i.e. out of the plane of photonic crystal slab [3]. Other methods include topology optimization [4], Wannier basis design [5], and bridged waveguide intersection [6]. The design of PhC waveguide crossings is generally based on cavity resonators which have inherently narrow bandwidth. The bandwidth can be increased by decreasing the Q-factor of the cavity resulting in lower transmission of the crossing. Nevertheless, the cross-talk levels of these designs are typically lower than $-30dB$. For silicon-on-insulator (SOI) waveguide crossings, different methods based on multimode interference [7, 8], mode expander [9], and wavefront matching [10] have been reported. Wavefront matching method has a very large footprint compared with multimode interference methods. The waveguide crossing mechanism based on impedance matched metamaterial have also been proposed [11]. This method has low bandwidth since it is based on negative refractive index metamaterial. To the best our knowledge, crossing of multiple waveguides at single intersection and multimode waveguide crossing have not been reported with methods of [1-6, 9-11]. New methods supporting the crossing of multiple waveguides based on inverse-design [12] and the MFE lens [13] have been investigated. Multimode waveguides play an important role in PICs and variety of devices are proposed based on them such as optical filters [14-16], power splitters [17, 18], polarization splitters [19, 20], sensors [21, 22], (de)multiplexers [23-26], switches [27-29], and wavelength converter [30]. Therefore, designing multimode waveguide crossings is vital in PICs and they have been introduced based on multimode-interference couplers [31, 32], subwavelength asymmetric Y-junction [33], and the MFE lens [34]. There has been no report of multiple waveguides crossing at an intersection with methods of [31-33]. However, the MFE lens supports the crossing of multiple multimode waveguides at an intersection with high bandwidth.

In this paper, it is demonstrated that the intersection of three single-mode or multimode waveguides can be implemented with MFE lens for transverse magnetic (TM) mode. Conventionally in PhCs, the TM mode is characterized by the electric field intensity being parallel to the rods and perpendicular to the plane of electromagnetic wave propagation and the transverse electric (TE) mode is characterized by the electric field intensity being parallel to the plane of electromagnetic wave propagation [35]. This paper presents, for the first time to the authors' knowledge, the implementation of MFE lens with concentric ring-based and radial-based structures instead of graded photonic crystals [13, 34]. The Si/SiO₂ multilayer with high refractive index contrast is adopted to implement the refractive index profile of the MFE lens. It is possible to realize metamaterials with intermediate refractive indices of the two constituent materials with the multilayer structure. The Si/SiO₂ is compatible with Complementary-Metal-Oxide-Semiconductor (CMOS) technology and reduces the cost of PIC development [36].

The refractive index of the MFE lens is given by [34]

$$n_{lens}(r) = \frac{2 \times n_{min}}{1 + (r/R_{lens})^2} \quad , \quad (0 \leq r \leq R_{lens}) \quad (1)$$

where n_{\min} is the minimum refractive index of the lens at its edge, R_{lens} is the radius of the lens and r is the radial distance from the center of the lens. In order to minimize the reflection at the lens interface, the n_{\min} should be equal to the environment refractive index [37]. Radiation of the point source on the surface of the lens, due to the lens's spatial variation of the refractive index, is focused on the diametrically opposite point of the lens. Fig. 1(a) shows the simple intersection of three waveguides. The crosstalk is substantial in this case and the signal is very weak in the intended output waveguide. In Fig. 1(b) the concept of intersection based on the ring-based multilayer MFE is shown. In gradient index (GRIN) lenses light propagates along a curved trajectory. In these figures, power streamlines are used to visualize the average power flow.

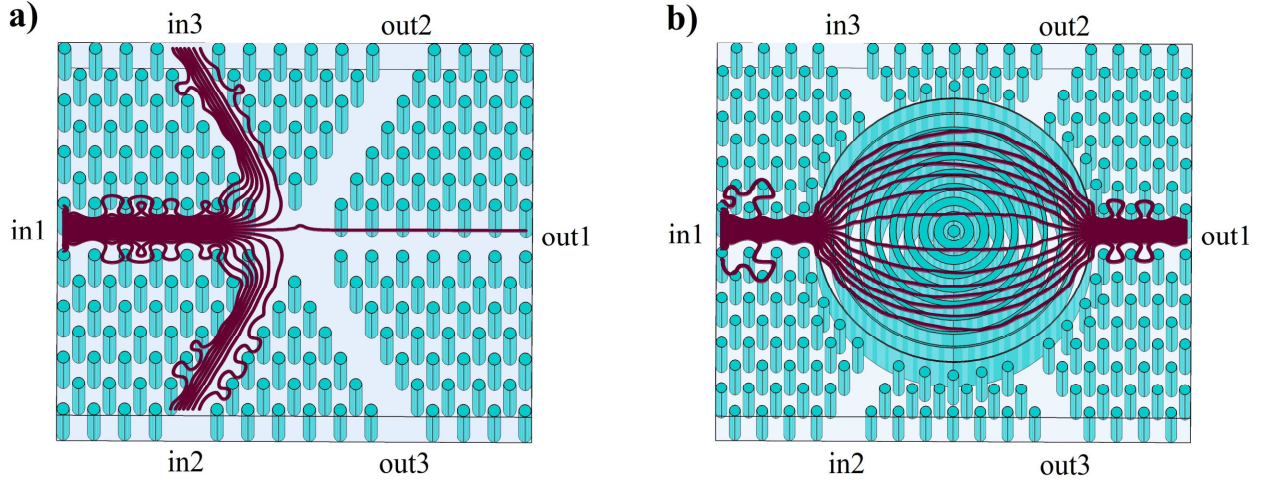


Fig. 1. Design concept. The flow of power is illustrated in the simple intersection of three waveguides in (a) and similarly with multilayer MFE lens as crossing medium in (b). The rods and inclusion layers of Si are embedded in SiO_2 background.

2. Multilayer GRIN lens design

The effective medium theory (EMT), also known as the effective medium approximation (EMA), is a homogenization method for determining the optical properties of composite materials based on the volume averaged fields. In the long-wavelength limit, where the wavelength of operation is considerably larger than the structure size, the wave does not resolve the subwavelength structure. In addition, Mie scattering and Bragg diffraction are negligible when the width of the layers and the duty cycle of the layered structure is well below the wavelength of the incident wave [38]. When these conditions are met, the structure can be considered as a homogeneous medium. The effective refractive index of the two-phase composite material depends on the ordered arrangement of the inclusions in the host to the electric field direction [39-42]. When the inclusions are arranged parallel to the electric field, the effective refractive index is approximated by [39]

$$n_{eff, TM}^2 = f_{inc} n_{inc}^2 + (1 - f_{inc}) n_{host}^2 \quad (2)$$

where n_{inc} , n_{host} , and $n_{eff,TE}$ are the refractive indices of the inclusion, host, and effective medium for TE mode, respectively. And filling factor, f_{inc} , is the fraction of the total volume occupied by inclusions. When the inclusions are arranged perpendicular to the electric field, the effective refractive index is given by [39]

$$n_{eff,TE}^2 = \frac{n_{inc}^2 n_{host}^2}{f_{inc} n_{host}^2 + (1 - f_{inc}) n_{inc}^2} \quad (3)$$

where $n_{eff,TE}$ is the refractive index of the effective medium for TE mode. When the comprising materials are isotropic, the dependence of the effective refractive index on the polarization is called form birefringence [43] and has interesting applications [44-46]. Form birefringent structures have high refractive index difference of TE and TM polarizations, Δn , compared to the naturally birefringent materials. Furthermore, the magnitude of Δn can be adjusted by the duty cycle and the shape of the structure [47].

Multilayer structures could be used to implement GRIN medium [36], metamaterials [48, 49], hyperlenses [50, 51], or invisibility cloaks [52, 53]. It is worth mentioning that there is no natural material exhibiting cylindrical anisotropy, however, it can be realized with multilayer metamaterials composed of isotropic materials [51]. The EMT can be used to calculate the refractive index of the multilayer structures ensuring that the thickness of each layer is much less than the incident wavelength and a sufficient number of layers is used [52]. By varying the filling factor of the inclusion material it is possible to control the effective refractive index of the structure. In this paper, the MFE lens is implemented by two different multilayer structures with homogeneous isotropic materials. The first structure is the ring-based multilayer MFE lens composed of concentric rings alternatively being Si or SiO₂ with a gradually decreasing filling factor. Here Si and SiO₂ are considered as the inclusion and host, respectively. Using the same materials for implementation of the PhC and MFE lens greatly simplify the fabrication process [54]. Our procedure for designing the ring-based MFE lens is to divide it into concentric cylindrical layers of equal width. For calculating the width of inclusion annulus in the i -th layer Eq. 2 is rearranged as

$$f_{inc} = \frac{n_{eff,TE}^2 - n_{host}^2}{n_{inc}^2 - n_{host}^2} \quad (4)$$

The filling factor for the i -th layer is $f_{inc} = A_{inc} / A_i$ where $A_{inc} = 2\pi r_i dr_{inc}$ and $A_i = 2\pi r_i dr$ are areas of inclusion and the i -th layer, respectively. The width of the layers, dr , is kept constant in our design. Consequently, the width of the inclusion layer, dr_{inc} , is calculated by the following equation:

$$dr_{inc} = \frac{n_{eff,TE}^2 - n_{host}^2}{n_{inc}^2 - n_{host}^2} dr \quad (5)$$

For the first layer $f_{inc} = \pi dr_{inc}^2 / \pi dr^2$ is used instead of Eq. 5. This procedure can also be applied to the design of lamellar multilayer GRIN medium.

Similar to the previous method, in the design of radial-based structure, the lens is divided into concentric cylindrical layers of equal width. Then each layer is divided into the desired number of equal annular sectors. In each annular sector, the filling factor is realized by inclusion of a sector with the same radii but smaller central angle. The inclusion sector is located at the center of the annular sector. Then the corners of consecutive inclusion sectors lying on the same radius are interpolated to form a radial rod.

3. Numerical simulation and discussion

The two-dimensional (2D) simulations were performed with Comsol MultiphysicsTM to verify the MFE lens's performance. The intersection of channel waveguides based on MFE lens is investigated in [34]. In our design, PhC waveguides are considered, therefore, the MFE lens is surrounded by PhC structure. Consequently, optical waves can only pass through the ports, so the performance of the MFE lens and scattering parameters can be investigated more precisely. The PhC structure consists of the 2D triangular lattice of cylindrical *Si* rods surrounded by *SiO₂* as host [55, 56]. In simulations, the refractive indices of *Si* and *SiO₂* are considered as 3.45 and 1.45, respectively. The lattice constant is $a = 465\text{nm}$ and rods have a radius of $r = 0.2a$ [57]. This PhC structure has a bandgap in TM mode covering S, C, L, and U optical communication bands. Although this paper focuses on designing of multilayer MFE lens for the TM mode, it is also possible to design the MFE lens for the TE mode with the method described in the previous section. In our design, to avoid reflection, the MFE lens's refractive index changes radially from 2.9 at the center to 1.45 at the edge of the lens to match the refractive index of the host material. The multilayer MFE lens is designed with the method described in the previous section. The approximation method from 3D model to 2D model is based on simple area averaging of *Si* and *SiO₂* layers. This approximate method does not consider the evanescent mode in claddings, however, it has been validated in [34, 39, 58, 59].

3.1 Concentric ring-based MFE lens

The ring-based lens with the radius of $2.56\mu\text{m}$ is divided into 10 cylindrical layers. The average refractive index of each layer is mapped to the width of the inclusion layer determined by Eq. (5). The width of inclusion layers decreases towards the edge of the lens indicating the decrease of the effective refractive index of the MFE lens.

Fig. 2 illustrates the computational domain of the simulation. To limit the number of simulations, the symmetrical computational domain is employed. One of the important factors considered in the construction of the computational domain is its size. Therefore, different domain truncation methods such as the perfectly matched layer (PML) or scattering boundary condition (SBC) are used to truncate the computational domain. In order to reduce the spurious reflection, the PhC waveguides are terminated by PhC-based PML. The PML domain surrounded by PhC structure is called PhC-based PML [60]. PhC-based PML is more effective compared to the conventional PML because the wave in the PhC-based PML region experiences the same refractive index contrast as in the PhC region [60] and moreover, the shape of the wave is preserved reducing the reflection from the ports [61]. Truncating the waveguide ends to SBC instead of PML, distorts the scattering parameters calculation with substantial reflection from the ports.

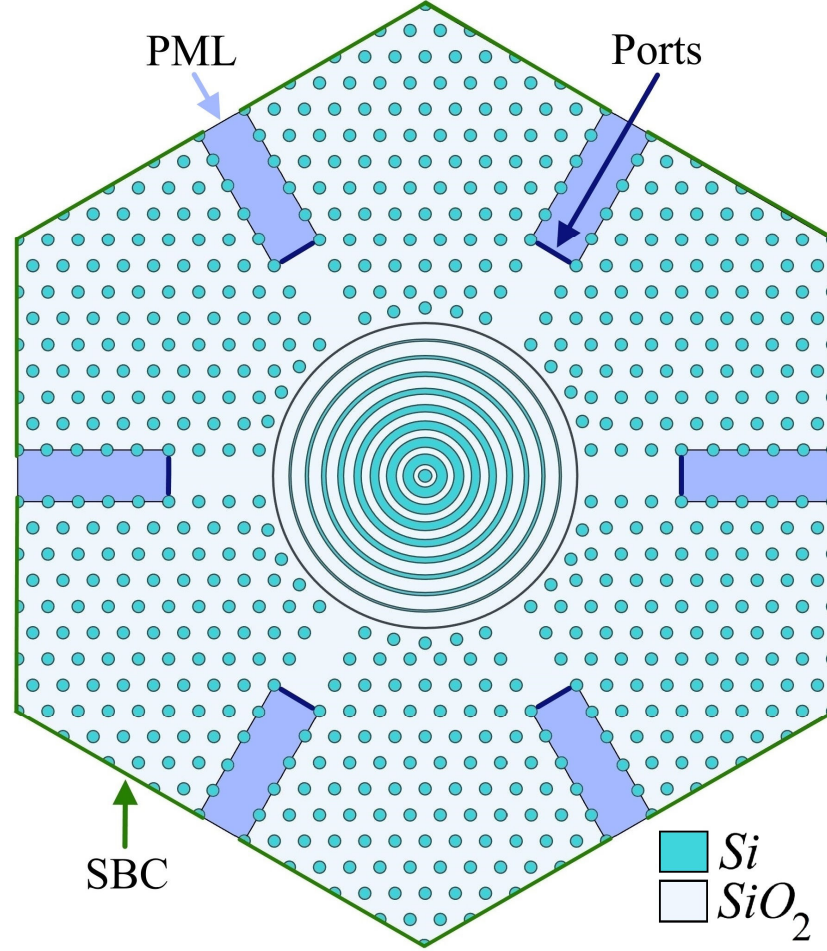


Fig. 2. Computational Domain. PhC-based PML and SBC are used to truncate the computational domain. All the rods and inclusion layers are Si and the host is SiO₂.

The transverse cross-section of the designed ring-based MFE lens is shown in Fig. 3(a). The filling factor of each inclusion layer is displayed numerically and graphically in the upper part of the Fig. 3(a). And the lower part of the Fig. 3(a) shows that the lens is divided into ten concentric cylindrical layers. The inclusion layers of Si are located in the center of cylindrical layers. Upper and lower claddings are SiO₂. Fig. 3(b) illustrates the propagation of TM mode signal at $1550nm$ passing through the ring-based MFE lens where the return loss of $-14.2dB$, insertion loss of $0.05dB$, and crosstalk levels below $-20.5dB$ are achieved. The waveguides are formed by removing one row of rods, so they only support TM₀. The scattering parameters of the ring-based 10-layer intersection are shown in Fig. 4(a). The eight transmission bands with a transmission of higher than $-3dB$ and linear phase response are highlighted. The number of layers and the space between the last layer and the waveguides are optimized to cover the entire C-band. In the C-band, the return loss of below $-11.2dB$, the average insertion loss of $0.2dB$, and crosstalk levels below $-17.4dB$ are achieved. Furthermore, the intersection covers about 80% of the U-band. Four of the MFE lens's modes are also presented in Fig. 4(b). The mode B is the prevalent mode of the lens in the C-band with lower insertion loss and crosstalk levels. For the mode D, although the transmission is higher than $-3dB$

the phase response is nonlinear and is not considered in the transmission band. The analytical study of the MFE lens's modes has been addressed in [62, 63]. The effect of device geometry errors was simulated to evaluate the tolerance of the concentric ring-based MFE lens to fabrication errors. The proposed structure can tolerate the variation in width of the inclusion layers of up to $\pm 5nm$ with the maximum excess insertion loss of $1.7dB$ in the C-band.

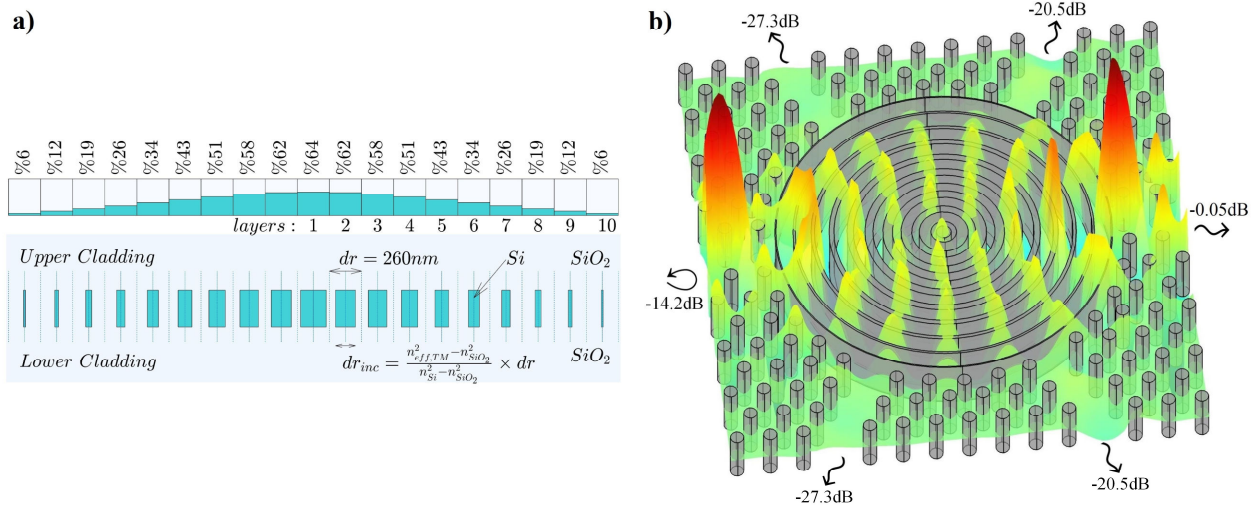


Fig. 3. Concentric ring-based MFE lens. a) The transverse cross-section of the designed ring-based MFE lens. The filling factor of each inclusion layer is displayed numerically and graphically in the upper part of this figure. And the lower part of this figure shows the inclusion layers of Si surrounded by SiO_2 . The upper and lower cladding are SiO_2 . b) Electric field distribution of 3×3 intersection based on concentric cylindrical multilayer MFE lens at $1550nm$.

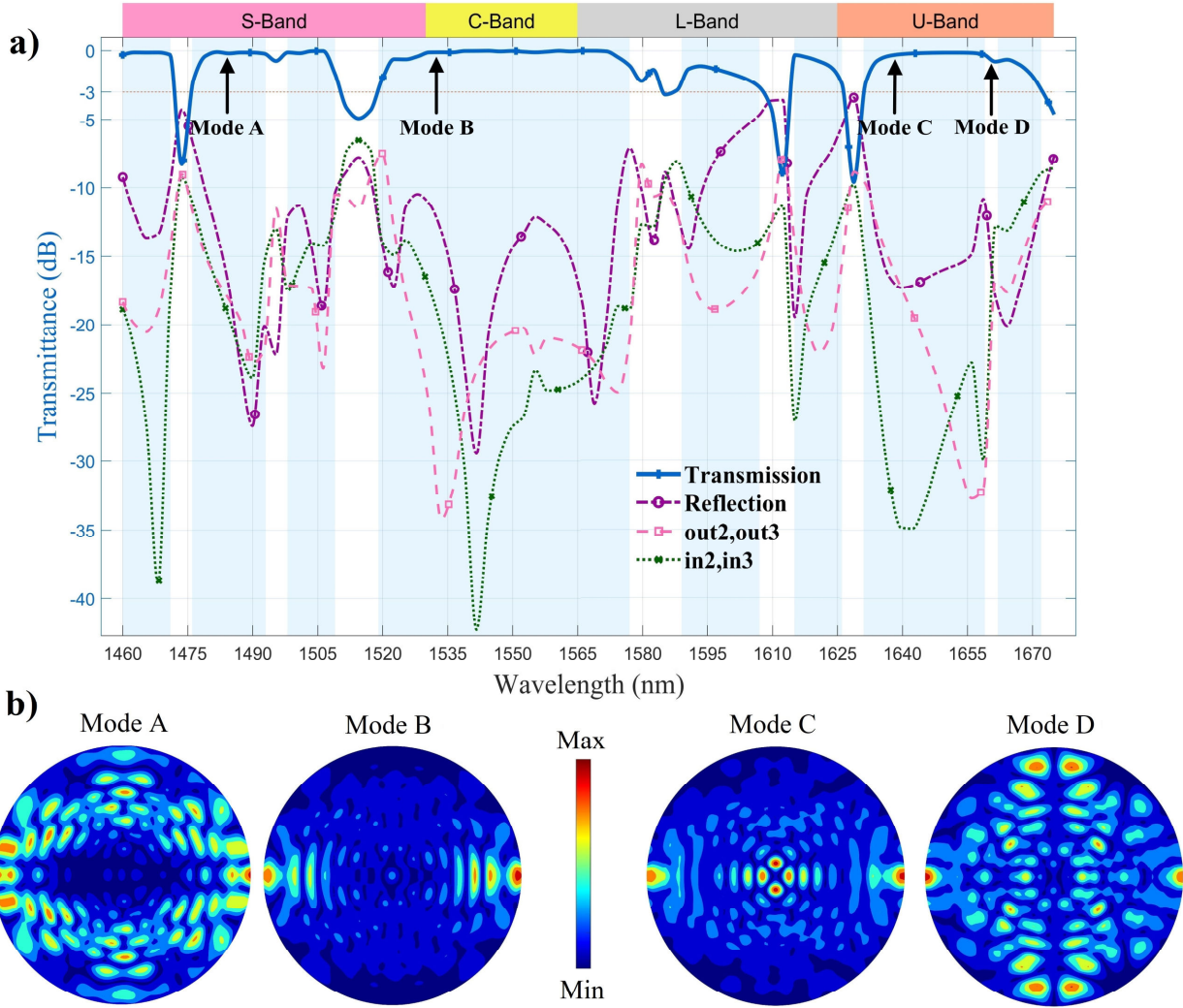


Fig. 4. Scattering parameters and modes. a) Scattering parameters of the designed ring-based multilayer intersection. b) Electric field distribution of selected modes of the MFE lens.

3.2 Radial-based MFE lens

An alternative approach in the implementation of the refractive index profile of the MFE lens is radial multilayers [50, 64]. The procedure described in the previous section is used for calculating the radial layers' geometry of the MFE lens with the radius of $2.56\mu\text{m}$ illustrated in Fig.5 (a). The designed gourd-shaped radial rods of Si and ten annular layers are shown in this figure. The radial rods of Si are surrounded by SiO_2 . The angle between consecutive radial rods is 7.5° . The first layer is designed similar to the ring-based design procedure resulting in a gap between the first layer and the radial rods. In order to satisfy the long-wavelength limit condition, the number of radial rods is increased towards the edge of the lens. As described in previous section, each layer is divided into a number of equal annular sectors. Moving from the center towards the edge of the lens, the number of annular sectors in each layer is doubled to double the number of rods in that layer.

However, to ease the fabrication limitations, after four layers the number of sectors is kept constant. Increasing the number of radial rods results in thinner rods and reduction of gourd shape sections' curvature, hence the fabrication constraints dictate the number of radial rods. The radial rod consists of gourd-shaped sections and one long graduated tip. The rods added in the second layer have triple gourd-shaped sections. However, the rods added in the third and fourth layers have double and single gourd-shaped sections. The rods added in the fifth layer only have a long graduated tip. The electric field distribution of the radial-based intersection is shown in the Fig. 5(b) at $1487nm$.

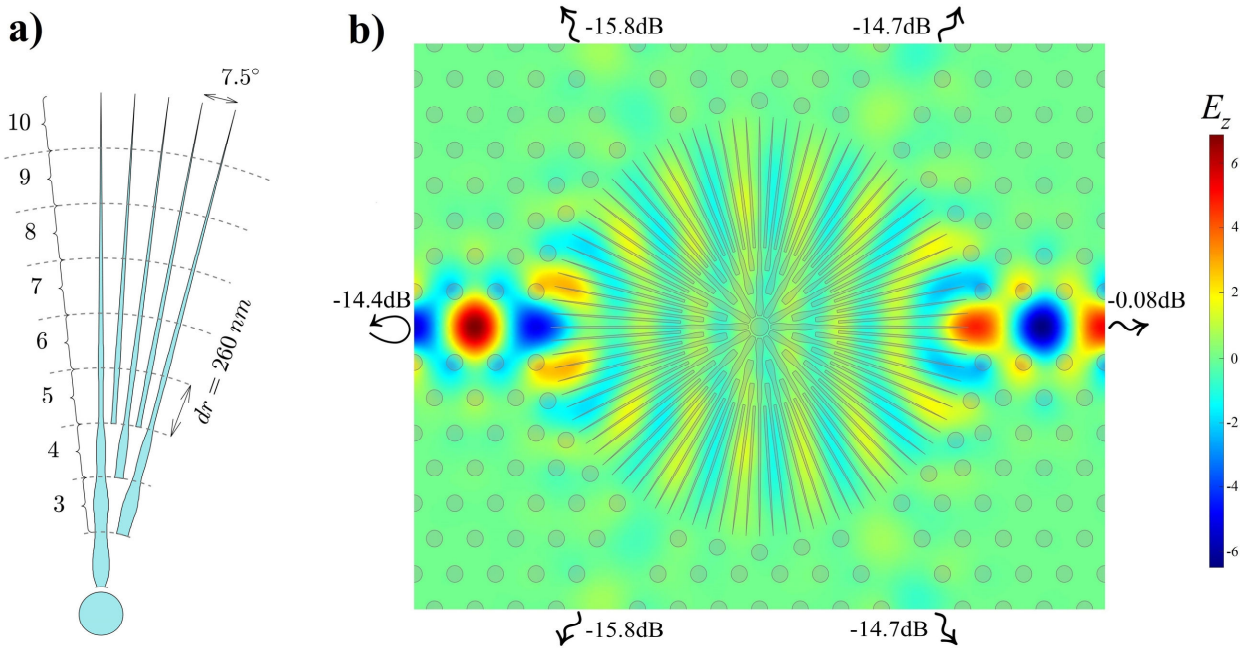


Fig. 5. Radial-based MFE lens. a) Geometry of a radial rods of Si and annular layers. The radial rods of Si are surrounded by SiO_2 . b) Electric field distribution of radial-based multilayer intersection at $1487nm$.

The scattering parameters of the radial-based intersection are illustrated in Fig. 6(a). The six transmission bands with transmission higher than $-3dB$ and linear phase response are highlighted. In Fig. 6(b), the radial-based lens's modes are presented which are different from the ring-based lens. The number of gourd-shaped radial rods in each layer is optimized to cover the entire C-band. In the C-band, the return loss of below $-4.3dB$, the average insertion loss of $1.5dB$, and crosstalk levels below $-10.8dB$ are achieved. Contrary to the ring-based design, it covers the entire U-band but with higher insertion loss. It also covers about 58% of the L-band. To provide a better understanding of the light pulse propagation through the radial-based MFE lens, a movie is presented at [65]. This video is created by Lumerical™ FDTD simulation software. The central frequency of the input pulse is $185.173THz$ and its bandwidth is $41.364THz$. In Fig. 7, the transmission capability of the two presented designs are compared. Both of the ring-based and radial-based multilayer intersections successfully cover the entire C-band. Although the ring-based lens has a better response in the C-band and lower insertion loss, the radial-based lens covers almost the entire U-band and has wider transmission bands. The radial-based MFE lens can tolerate the

random variation in width of the radial rods of up to $\pm 5nm$ with the maximum excess insertion loss of $1.1dB$ in the C-band.

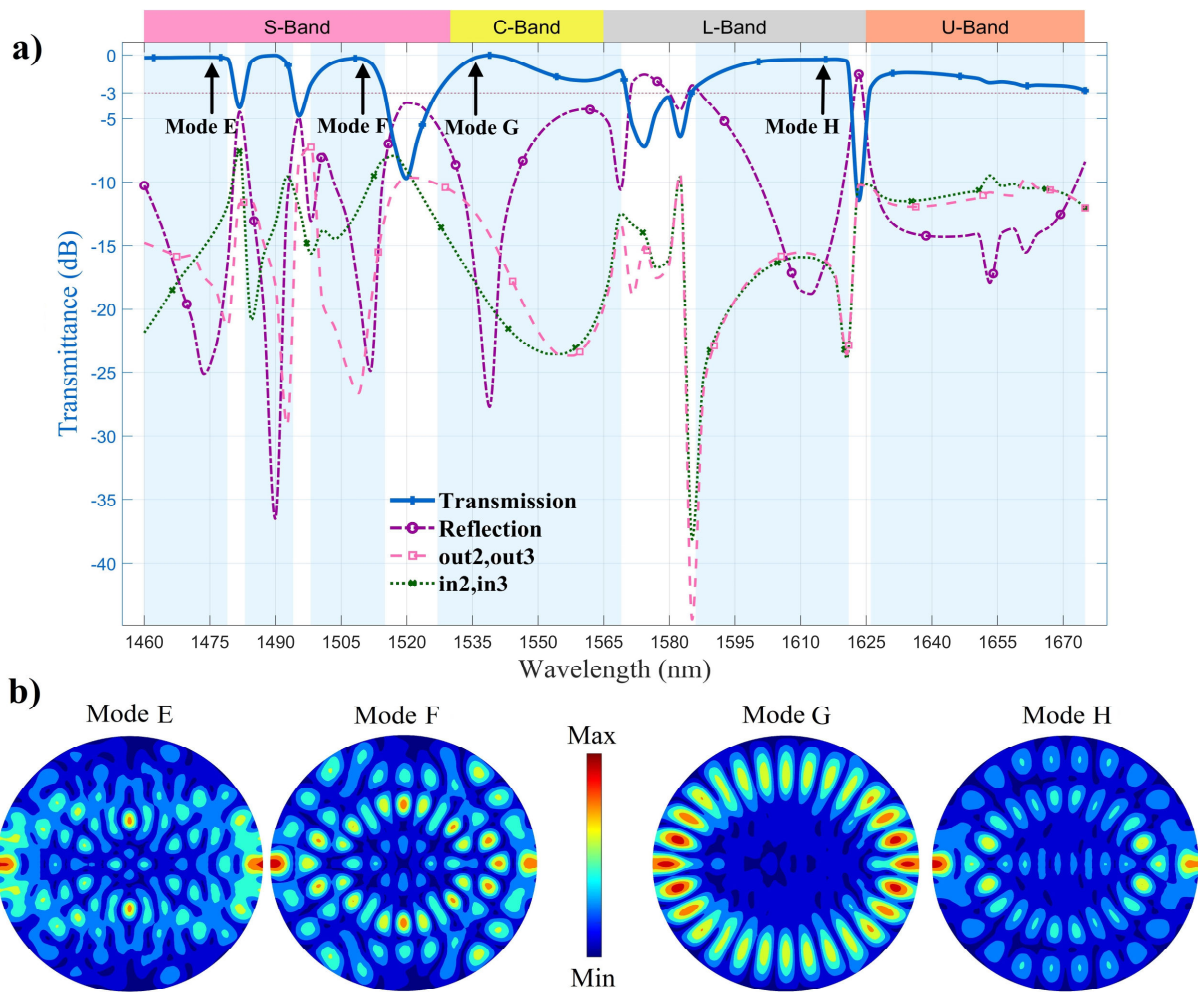


Fig. 6. Scattering parameters and modes. a) Scattering parameters of the designed radial-based multilayer intersection. b) Electric field distribution of selected modes of the MFE lens.

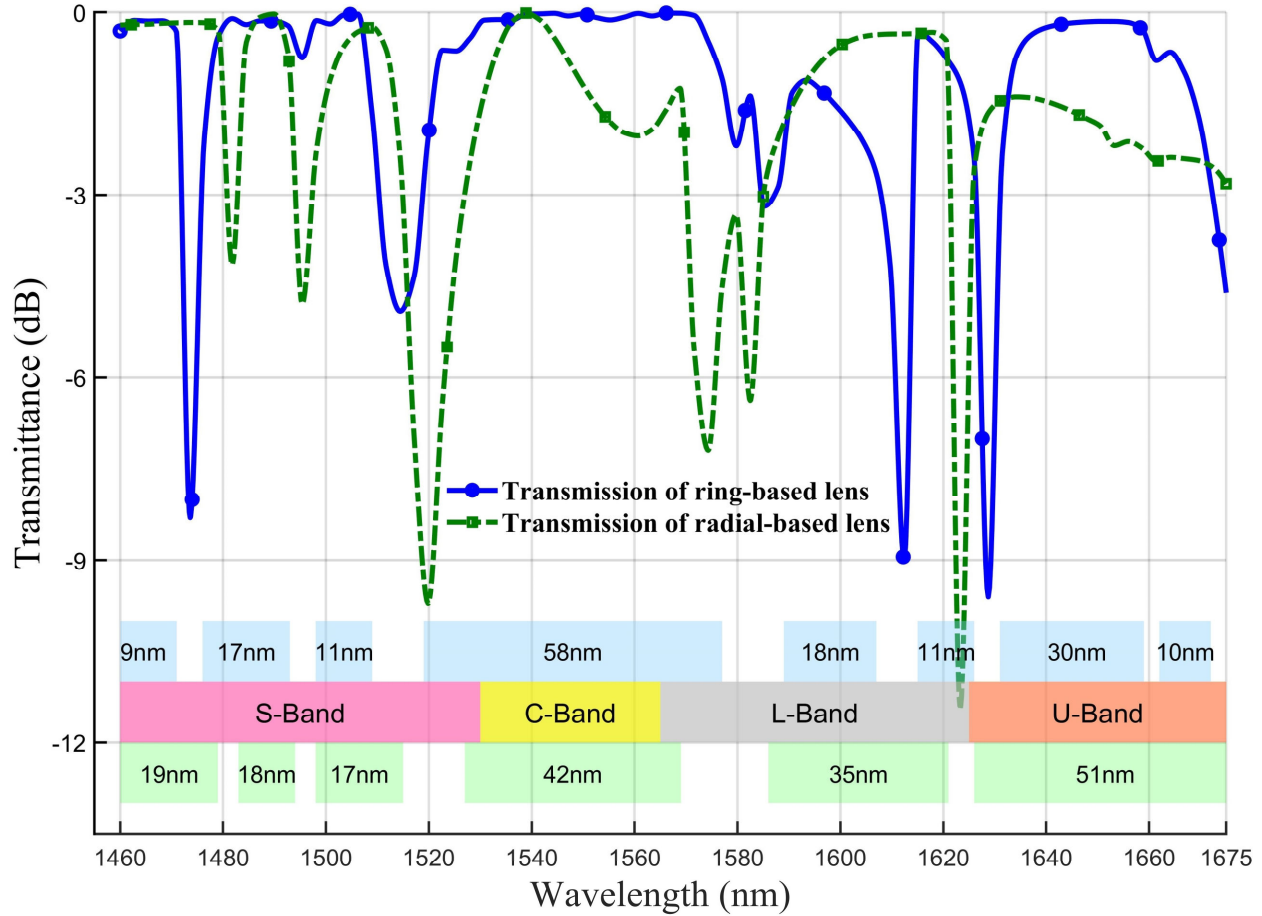


Fig. 7. Comparison of the ring-based and radial-based multilayer intersections' transmission. Blue and green horizontal bars specify the bands with the acceptable transmission for ring-based and radial-based intersections, respectively. Each transmission band's bandwidth is determined.

3.3 Multimode waveguide crossing

The MFE lens can also support the transmission of higher modes. In this paper, transmission of TM_0 and TM_1 through the ring-based MFE lens is also investigated. However, the simulations, not presented here, show that the MFE lens can support higher modes simply by increasing the waveguides' width and the lens's radius. The multimode photonic crystal waveguides (PhCW) are obtained by removing multiple neighboring rows of rods [18, 24, 66]. In our simulations, three consecutive rows are removed to form a multimode PhCW. The electric field distribution for TM_0 and TM_1 are illustrated in Fig. 8 at the wavelength of $1550nm$. The scattering parameters of the multimode waveguide intersection are illustrated in Fig. 9. As the width of the waveguide increases the optical confinement decreases, resulting in lower insertion loss and lower crosstalk levels [8]. The three transmission bands where both TM_0 and TM_1 have transmissions higher than $-3dB$ and linear phase responses are highlighted. In the C-band, the return loss of below $-14.8dB$, the average insertion loss of $0.17dB$, and crosstalk levels below $-24.2dB$ are achieved.

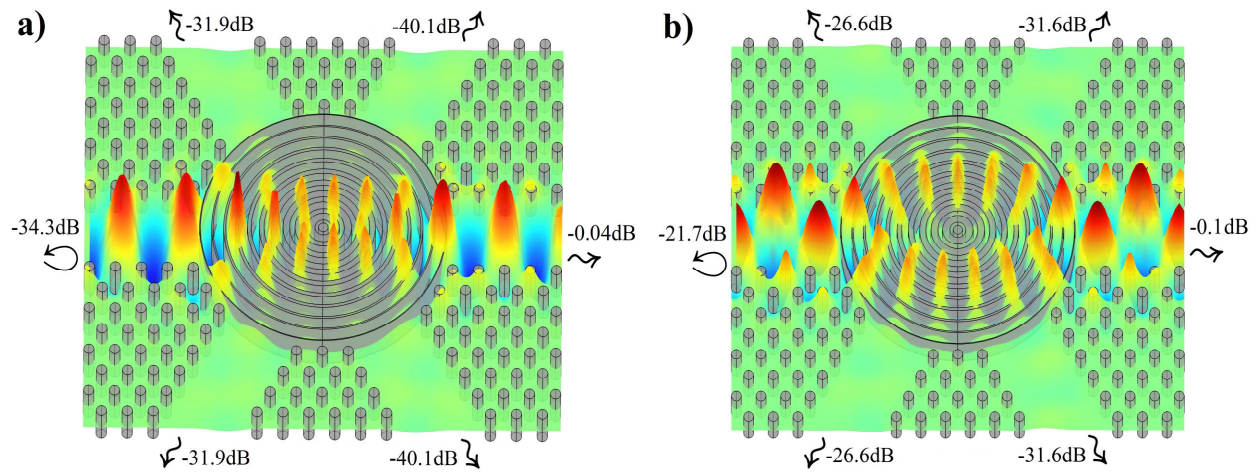


Fig. 8. Multimode ring-based multilayer intersection. The electric field distribution is illustrated at the wavelength of 1550nm for a) TM_0 and b) TM_1 modes.

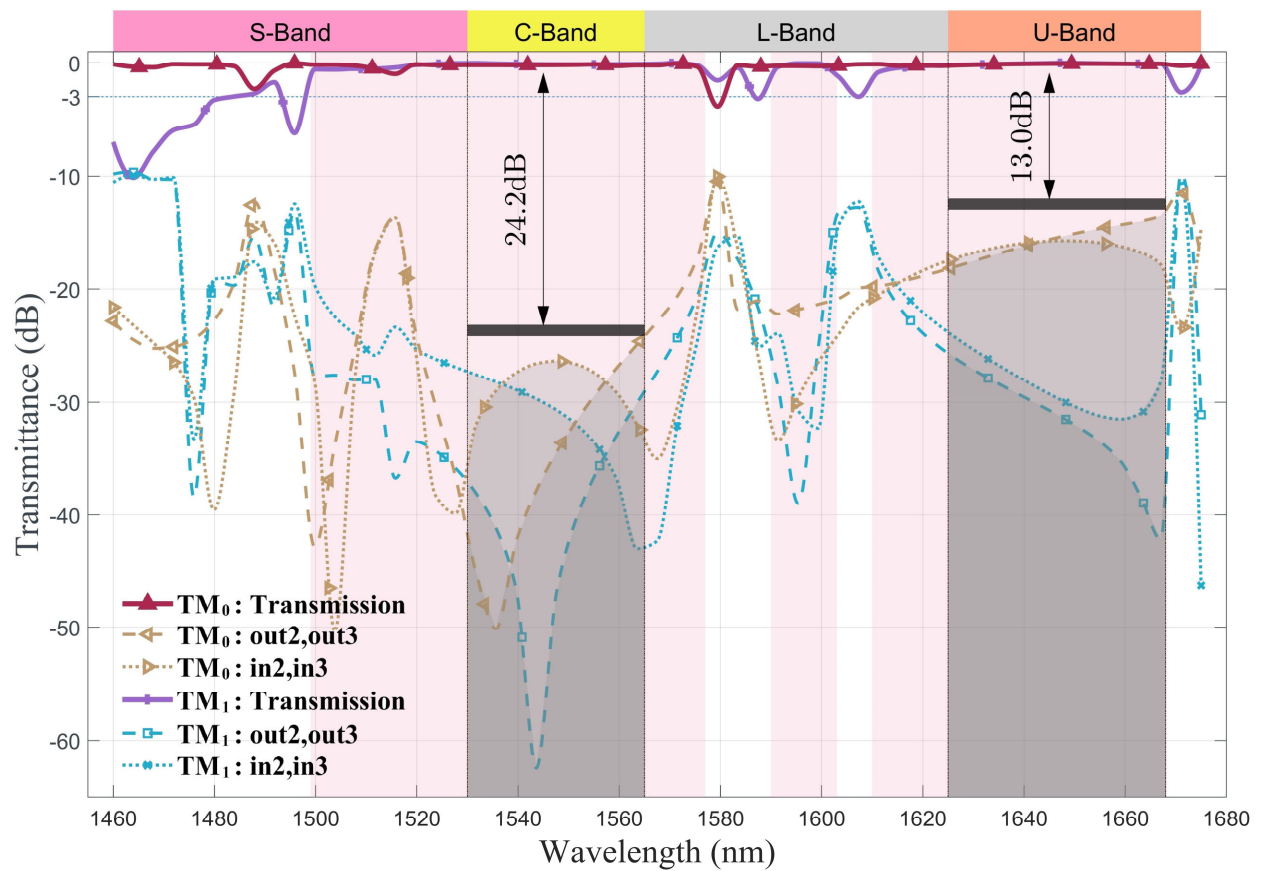


Fig. 9. Comparison of the multimode intersections' transmission. The transmission bands covering both TM_0 and TM_1 modes are highlighted.

The characteristics of the waveguide crossings of the references discussed in introduction section are summarized in Table 1. The crossing mechanism, insertion loss, central wavelength, bandwidth, crosstalk, and footprint are compared in this table. It has also been specified whether the intersection of multiple waveguides and intersection of multimode waveguides are reported in the literatures mentioned in the introduction section. Some of the specifications are not explicitly given in the references, therefore they are extracted from the figures. Some references used normalized frequency based on lattice constant. In order to provide tangible specifications, when the lattice constant was not given, it was calculated in a way that the center of the crossing's passband lies in the center of the photonic band gap. Only the crossings based on the MFE lens support the crossing of multiple multimode waveguides at an intersection. Compared to the other works, the footprint of the presented multimode waveguide crossing is smallest.

Table 1. Characteristics of the waveguide crossings

reference	Year	Crossing Mechanism	Polarization	Waveguide Type	Insertion Loss (dB)	λ_{center} (nm)	Bandwidth (nm)	Cross-talk(dB)	Footprint (μm^2)	intersection of multiple waveguides reported	intersection of multimode waveguides reported
[1]	1998	Cavity	TM	PhC	-	1550	17	-34	1.2×1.2	No	No
[2]	2002	Cavity	TE	PhC	6	1306	4	-18	5.6×5.6	No	No
[3]	2007	Cavity	TE	PhC	0.91	1300	30	-30	3.6×3.6	No	No
[4]	2006	topology optimization	TE	PhC	2	1275	50	-22	1.8×2.2	No	No
[5]	2005	Cavity	TE	PhC	0.04	1550	33	-40	2.7×2.7	No	No
[6]	2012	Cavity	TM	PhC	0.09	1540	4.66	-18	3.65×3.65	No	No
[7]	2006	Multimode-interference	TE	Si waveguide	0.4	1550	100	-33	13×13	No	No
[8]	2010	Multimode-interference	TE	Si waveguide	0.21	1550	100	-38	5.5×5.5	No	No
[9]	2007	Mode expander	TE	Si waveguide	0.16	1550	40	-40	6×6	No	No
[10]	2007	Wavefront matching	TE/TM	Silica waveguide	0.35	1550	-	-35	120×230	No	No
[11]	2010	impedance matched metamaterials	TM	Si waveguide	0.04	-	-	-40	-	No	No
[12]	2017	Inverse-designed	TE	Silica waveguide	0.75	1550	80	-22.5	5.33×5.33	Yes	No
[13]	2018	MFE lens	TM	PhC	0.6 , 1.3	1561 , 1643	64 , 63	-16 , -18	7.6×7.6	Yes	No
[31]	2018	Multimode-interference	TE	Si waveguide	0.6	1560	60	-24	4.8×4.8	No	Yes
[32]	2016	Multimode-interference	TM	Si waveguide	1.5	1560	80	-18	29×29	No	Yes
[33]	2018	Asymmetric Y-junction	TE	Si waveguide	0.9	1560	80	-24	34×34	No	Yes
[34]	2018	MFE lens	TM	Si waveguide	0.3	1560	80	-20	14×14	Yes	Yes
radial-based MFE lens	this work	MFE lens	TM	PhC	1.1 , 2.1	1552 , 1649	42 , 51	-10 , -9	5.1×5.1	No	Yes
concentric ring-based MFE lens	this work	MFE lens	TM	PhC	0.2 , 0.15	1538 , 1638	78 , 57	-14 , -13	4.65×4.65	Yes	Yes

4. Conclusion

The MFE lens, due to its imaging properties, is utilized as the intersection of multiple waveguides supporting any number of allowed modes. We believe that for the first time the MFE lens is implemented as ring-based and radial-based multilayer metamaterial comprising periodic Si and SiO₂ layers in this work. The simulations show that the all-dielectric metamaterial-based MFE lens can be used to implement broadband single-mode and multimode waveguide crossings with low insertion loss and low crosstalk levels. For the single-mode waveguide crossing, crosstalk levels below -17.4dB and the average insertion loss of 0.2dB , are achieved in the C-band. For the multimode waveguide crossing based on the MFE lens with $4.65 \times 4.65 \mu\text{m}^2$ footprint, crosstalk levels lower than -24.2dB and the average insertion loss of 0.17dB are obtained for both TM₀ and TM₁ modes in the C-band.

References

- [1] S.G. Johnson, C. Manolatou, S. Fan, P.R. Villeneuve, J. Joannopoulos, H. Haus, Elimination of cross talk in waveguide intersections, *Optics Letters*, 23 (1998) 1855-1857.
- [2] S. Lan, H. Ishikawa, Broadband waveguide intersections with low cross talk in photonic crystal circuits, *Optics letters*, 27 (2002) 1567-1569.
- [3] Z. Li, H. Chen, J. Chen, F. Yang, H. Zheng, S. Feng, A proposal for low cross-talk square-lattice photonic crystal waveguide intersection utilizing the symmetry of waveguide modes, *Optics communications*, 273 (2007) 89-93.
- [4] Y. Watanabe, Y. Sugimoto, N. Ikeda, N. Ozaki, A. Mizutani, Y. Takata, Y. Kitagawa, K. Asakawa, Broadband waveguide intersection with low-crosstalk in two-dimensional photonic crystal circuits by using topology optimization, *Optics express*, 14 (2006) 9502-9507.
- [5] Y. Jiao, S.F. Mingaleev, M. Schillinger, D.A. Miller, S. Fan, K. Busch, Wannier basis design and optimization of a photonic crystal waveguide crossing, *IEEE photonics technology letters*, 17 (2005) 1875-1877.
- [6] A.H. Khanmirzaei, M. Abrishamian, A bridged waveguide intersection in two-dimensional photonic crystal structures, *Optik-International Journal for Light and Electron Optics*, 123 (2012) 653-656.
- [7] H. Chen, A.W. Poon, Low-loss multimode-interference-based crossings for silicon wire waveguides, *IEEE photonics technology letters*, 18 (2006) 2260-2262.
- [8] C.-H. Chen, C.-H. Chiu, Taper-integrated multimode-interference based waveguide crossing design, *IEEE Journal of Quantum Electronics*, 46 (2010) 1656-1661.
- [9] W. Bogaerts, P. Dumon, D. Van Thourhout, R. Baets, Low-loss, low-cross-talk crossings for silicon-on-insulator nanophotonic waveguides, *Optics letters*, 32 (2007) 2801-2803.
- [10] Y. Sakamaki, T. Saida, T. Hashimoto, H. Takahashi, New optical waveguide design based on wavefront matching method, *Journal of Lightwave Technology*, 25 (2007) 3511-3518.
- [11] W. Ding, D. Tang, Y. Liu, L. Chen, X. Sun, Compact and low crosstalk waveguide crossing using impedance matched metamaterial, *Applied Physics Letters*, 96 (2010) 111114.
- [12] L. Lu, M. Zhang, F. Zhou, W. Chang, J. Tang, D. Li, X. Ren, Z. Pan, M. Cheng, D. Liu, Inverse-designed ultra-compact star-crossings based on PhC-like subwavelength structures for optical interconnect, *Optics Express*, 25 (2017) 18355-18364.
- [13] M.M. Gilarlue, S.H. Badri, H. Rasooli Saghaj, J. Nourinia, C. Ghobadi, Photonic crystal waveguide intersection design based on Maxwell's fish-eye lens, *Photonics and Nanostructures - Fundamentals and Applications*, 31 (2018) 154-159.
- [14] M. Mendez-Astudillo, H. Okayama, H. Nakajima, Silicon optical filter with transmission peaks in wide stopband obtained by anti-symmetric photonic crystal with defect in multimode waveguides, *Optics express*, 26 (2018) 1841-1850.
- [15] P. Sah, B.K. Das, Photonic bandpass filter characteristics of multimode SOI waveguides integrated with submicron gratings, *Applied optics*, 57 (2018) 2277-2281.

- [16] Q. Huang, K. Jie, Q. Liu, Y. Huang, Y. Wang, J. Xia, Ultra-compact, broadband tunable optical bandstop filters based on a multimode one-dimensional photonic crystal waveguide, *Optics express*, 24 (2016) 20542-20553.
- [17] Z. Han, S. He, Multimode interference effect in plasmonic subwavelength waveguides and an ultra-compact power splitter, *Optics communications*, 278 (2007) 199-203.
- [18] Y. Zhang, Z. Li, B. Li, Multimode interference effect and self-imaging principle in two-dimensional silicon photonic crystal waveguides for terahertz waves, *Optics Express*, 14 (2006) 2679-2689.
- [19] Y. Xu, J. Xiao, X. Sun, Compact polarization beam splitter for silicon-based slot waveguides using an asymmetrical multimode waveguide, *Journal of Lightwave Technology*, 32 (2014) 4282-4288.
- [20] Y. Shi, A compact polarization beam splitter based on a multimode photonic crystal waveguide with an internal photonic crystal section, *Progress In Electromagnetics Research*, 103 (2010) 393-401.
- [21] N. Skivesen, R. Horvath, H.C. Pedersen, Multimode reverse-symmetry waveguide sensor for broad-range refractometry, *Optics letters*, 28 (2003) 2473-2475.
- [22] G.C. Valley, G.A. Sefler, T.J. Shaw, Multimode waveguide speckle patterns for compressive sensing, *Optics letters*, 41 (2016) 2529-2532.
- [23] Y. Kou, X. Chen, Multimode interference demultiplexers and splitters in metal-insulator-metal waveguides, *Optics express*, 19 (2011) 6042-6047.
- [24] H.-J. Kim, I. Park, O. Beom-Hoan, S.-G. Park, E.-H. Lee, S.-G. Lee, Self-imaging phenomena in multi-mode photonic crystal line-defect waveguides: application to wavelength de-multiplexing, *Optics express*, 12 (2004) 5625-5633.
- [25] H. Xu, Y. Shi, Broadband Nine-Channel Mode-Division (de) Multiplexer Based on Densely Packed Multimode Waveguide Arrays, *Journal of Lightwave Technology*, 35 (2017) 4949-4953.
- [26] R.B. Priti, O. Liboiron-Ladouceur, A Reconfigurable Multimode Demultiplexer/Switch for Mode-Multiplexed Silicon Photonics Interconnects, *IEEE Journal of Selected Topics in Quantum Electronics*, (2018).
- [27] Y. Zhang, Y. He, Q. Zhu, C. Qiu, Y. Su, On-chip silicon photonic 2×2 mode-and polarization-selective switch with low inter-modal crosstalk, *Photonics Research*, 5 (2017) 521-526.
- [28] B. Stern, X. Zhu, C.P. Chen, L.D. Tzuang, J. Cardenas, K. Bergman, M. Lipson, On-chip mode-division multiplexing switch, *Optica*, 2 (2015) 530-535.
- [29] S. Wang, X. Feng, S. Gao, Y. Shi, T. Dai, H. Yu, H.-K. Tsang, D. Dai, On-chip reconfigurable optical add-drop multiplexer for hybrid wavelength/mode-division-multiplexing systems, *Optics letters*, 42 (2017) 2802-2805.
- [30] Y. Ding, J. Xu, H. Ou, C. Peucheret, Mode-selective wavelength conversion based on four-wave mixing in a multimode silicon waveguide, *Optics express*, 22 (2014) 127-135.
- [31] W. Chang, L. Lu, X. Ren, D. Li, Z. Pan, M. Cheng, D. Liu, M. Zhang, Ultracompact dual-mode waveguide crossing based on subwavelength multimode-interference couplers, *Photonics Research*, 6 (2018) 660-665.
- [32] H. Xu, Y. Shi, Dual-mode waveguide crossing utilizing taper-assisted multimode-interference couplers, *Optics letters*, 41 (2016) 5381-5384.
- [33] W. Chang, L. Lu, X. Ren, L. Lu, M. Cheng, D. Liu, M. Zhang, An Ultracompact Multimode Waveguide Crossing Based on Subwavelength Asymmetric Y-Junction, *IEEE Photonics Journal*, 10 (2018) 1-8.
- [34] H. Xu, Y. Shi, Metamaterial-Based Maxwell's Fisheye Lens for Multimode Waveguide Crossing, *Laser & Photonics Reviews*, 1800094.
- [35] S. Fan, J.N. Winn, A. Devenyi, J. Chen, R.D. Meade, J. Joannopoulos, Guided and defect modes in periodic dielectric waveguides, *JOSA B*, 12 (1995) 1267-1272.
- [36] T.-H. Loh, Q. Wang, J. Zhu, K.-T. Ng, Y.-C. Lai, Y. Huang, S.-T. Ho, Ultra-compact multilayer Si/SiO₂ GRIN lens mode-size converter for coupling single-mode fiber to Si-wire waveguide, *Optics express*, 18 (2010) 21519-21533.
- [37] L.H. Gabrielli, M. Lipson, Integrated Luneburg lens via ultra-strong index gradient on silicon, *Optics express*, 19 (2011) 20122-20127.
- [38] I. Staude, J. Schilling, Metamaterial-inspired silicon nanophotonics, *Nature Photonics*, 11 (2017) 274.
- [39] U. Levy, M. Nezhad, H.-C. Kim, C.-H. Tsai, L. Pang, Y. Fainman, Implementation of a graded-index medium by use of subwavelength structures with graded fill factor, *JOSA A*, 22 (2005) 724-733.
- [40] P.S. Neelakanta, *Handbook of electromagnetic materials: monolithic and composite versions and their applications*, CRC press 1995.
- [41] R. Bräuer, O. Bryngdahl, Design of antireflection gratings with approximate and rigorous methods, *Applied optics*, 33 (1994) 7875-7882.

- [42] H. Wang, X. Liu, L. Wang, Z. Zhang, Anisotropic optical properties of silicon nanowire arrays based on the effective medium approximation, *International Journal of Thermal Sciences*, 65 (2013) 62-69.
- [43] M. Born, E. Wolf, *Principles of optics: electromagnetic theory of propagation, interference and diffraction of light*, Elsevier 2013.
- [44] M. Lorente-Crespo, G. Ballesteros, C. Mateo-Segura, Transparent all-dielectric gradient index waveplates with compact profiles, *Applied Physics Letters*, 109 (2016) 111105.
- [45] M. Scheller, C. Jördens, M. Koch, Terahertz form birefringence, *Optics express*, 18 (2010) 10137-10142.
- [46] S. Pan, L. Tan, H.S. Kwok, Broadband reflective polarizers based on form birefringence for ultra-thin liquid crystal displays, *Optics express*, 25 (2017) 17499-17510.
- [47] F. Xu, R.-C. Tyan, P.-C. Sun, Y. Fainman, C.-C. Cheng, A. Scherer, Fabrication, modeling, and characterization of form-birefringent nanostructures, *Optics letters*, 20 (1995) 2457-2459.
- [48] X. Yang, J. Yao, J. Rho, X. Yin, X. Zhang, Experimental realization of three-dimensional indefinite cavities at the nanoscale with anomalous scaling laws, *Nature Photonics*, 6 (2012) 450.
- [49] C. Cortes, W. Newman, S. Molesky, Z. Jacob, Quantum nanophotonics using hyperbolic metamaterials, *Journal of Optics*, 14 (2012) 063001.
- [50] J. Sun, M.I. Shalaev, N.M. Litchinitser, Experimental demonstration of a non-resonant hyperlens in the visible spectral range, *Nature communications*, 6 (2015) 7201.
- [51] Z. Jacob, L.V. Alekseyev, E. Narimanov, Optical hyperlens: far-field imaging beyond the diffraction limit, *Optics express*, 14 (2006) 8247-8256.
- [52] Y. Huang, Y. Feng, T. Jiang, Electromagnetic cloaking by layered structure of homogeneous isotropic materials, *Optics express*, 15 (2007) 11133-11141.
- [53] X. Xu, Y. Feng, Y. Hao, J. Zhao, T. Jiang, Infrared carpet cloak designed with uniform silicon grating structure, *Applied Physics Letters*, 95 (2009) 184102.
- [54] R.B. Nielsen, M.D. Thoreson, W. Chen, A. Kristensen, J.M. Hvam, V. Shalaev, A. Boltasseva, Toward superlensing with metal-dielectric composites and multilayers, *Applied Physics B*, 100 (2010) 93-100.
- [55] Y.-F. Chau, T.-J. Yang, W.-D. Lee, Coupling technique for efficient interfacing between silica waveguides and planar photonic crystal circuits, *Applied optics*, 43 (2004) 6656-6663.
- [56] A. Håkansson, P. Sanchis, J. Sánchez-Dehesa, J. Martí, High-efficiency defect-based photonic-crystal tapers designed by a genetic algorithm, *Journal of Lightwave Technology*, 23 (2005) 3881.
- [57] P. Sanchis, J. Martí, A. Garcia, A. Martinez, J. Blasco, High efficiency coupling technique for planar photonic crystal waveguides, *Electronics Letters*, 38 (2002) 961-962.
- [58] L.H. Gabrielli, J. Cardenas, C.B. Poitras, M. Lipson, Silicon nanostructure cloak operating at optical frequencies, *Nature photonics*, 3 (2009) 461.
- [59] V.A. Tamma, J. Blair, C.J. Summers, W. Park, Dispersion characteristics of silicon nanorod based carpet cloaks, *Optics express*, 18 (2010) 25746-25756.
- [60] M. Koshiba, Y. Tsuji, S. Sasaki, High-performance absorbing boundary conditions for photonic crystal waveguide simulations, *IEEE Microwave and wireless components letters*, 11 (2001) 152-154.
- [61] J.-P. Berenger, A perfectly matched layer for the absorption of electromagnetic waves, *Journal of computational physics*, 114 (1994) 185-200.
- [62] H. Rosu, M. Reyes, Electromagnetic modes of Maxwell fish-eye lens, *Il Nuovo Cimento D*, 16 (1994) 517-522.
- [63] U. Leonhardt, Perfect imaging without negative refraction, *New Journal of Physics*, 11 (2009) 093040.
- [64] A. Sayanskiy, S. Glybovski, V.P. Akimov, D. Filonov, P. Belov, I. Meshkovskiy, Broadband 3-D Luneburg Lenses Based on Metamaterials of Radially Diverging Dielectric Rods, *IEEE Antennas and Wireless Propagation Letters*, 16 (2017) 1520-1523.
- [65] H. Rasooli Saghai, S.H. Badri, Radial-based multilayer Maxwell's fish-eye lens as a waveguide Crossing, *Mendeley Data*, v2, (2018).
- [66] H.-H. Tao, R.-J. Liu, Z.-Y. Li, S. Feng, Y.-Z. Liu, C. Ren, B.-Y. Cheng, D.-Z. Zhang, H.-Q. Ma, L.-A. Wu, Mapping of complex optical field patterns in multimode photonic crystal waveguides by near-field scanning optical microscopy, *Physical Review B*, 74 (2006) 205111.